

## FAST GYROSYNCHROTRON CODES

GREGORY D. FLEISHMAN<sup>1,2</sup> AND ALEXEY A. KUZNETSOV<sup>3,4</sup>

<sup>1</sup> Center For Solar-Terrestrial Research, New Jersey Institute of Technology, Newark, NJ 07102, USA

<sup>2</sup> Ioffe Physico-Technical Institute, St. Petersburg 194021, Russia

<sup>3</sup> Armagh Observatory, Armagh BT61 9DG, Northern Ireland, UK

<sup>4</sup> Institute of Solar-Terrestrial Physics, Irkutsk 664033, Russia

Received 2010 March 21; accepted 2010 May 3; published 2010 September 7

### ABSTRACT

Radiation produced by charged particles gyrating in a magnetic field is highly significant in the astrophysics context. Persistently increasing resolution of astrophysical observations calls for corresponding three-dimensional modeling of the radiation. However, available exact equations are prohibitively slow in computing a comprehensive table of high-resolution models required for many practical applications. To remedy this situation, we develop approximate gyrosynchrotron (GS) codes capable of quickly calculating the GS emission (in non-quantum regime) from both isotropic and anisotropic electron distributions in non-relativistic, mildly relativistic, and ultrarelativistic energy domains applicable throughout a broad range of source parameters including dense or tenuous plasmas and weak or strong magnetic fields. The computation time is reduced by several orders of magnitude compared with the exact GS algorithm. The new algorithm performance can gradually be adjusted to the user's needs depending on whether precision or computation speed is to be optimized for a given model. The codes are made available for users as a supplement to this paper.

**Key words:** methods: numerical – radiation mechanisms: non-thermal – radio continuum: planetary systems – stars: flare – Sun: flares – Sun: radio radiation

**Online-only material:** supplemental data (tar.gz)

### 1. INTRODUCTION

Radiation produced by charged particles moving in magnetic fields (magnetobremssstrahlung) plays an exceptionally important role in astrophysics, making a dominant contribution to radio emission in most of the astrophysical objects, a major contribution to gamma-ray and X-ray emission (in compact objects, supernova remnants (SNRs), and gamma-ray burst sources), and an important contribution to the IR/optical/UV (in active galactic nuclei or extragalactic jets), which implies a necessity of its calculation in highly diverse conditions specific to the object or phenomenon under study. A straightforward way of performing such computations is the use of exact formulae for the emissivities and absorption coefficients (Eidman 1958, 1959; Melrose 1968; Ramaty 1969) that are valid for arbitrary conditions (when the magnetic field changes in space only smoothly and no quantum effect is important).

However, these exact formulae are cumbersome and computationally extremely slow, especially when high harmonics of the gyrofrequency are involved (that is, when the emission frequency is much larger than the gyrofrequency). This is why a number of simplified approaches have been developed whose applicability regions and/or accuracy are limited. For example, for ultrarelativistic emitting particles a so-called synchrotron approximation (Korchak & Terletsky 1952; Getmantsev 1952; Korchak 1957; Syrovatskii 1959; Razin 1960) is valid (see Ginzburg & Syrovatskii 1965, 1969, for review), which is often sufficient for such astrophysical objects as SNRs or radio galaxies.

For the gyrosynchrotron (GS) regime, when nonrelativistic and mildly relativistic particles are involved—a typical case, e.g., for solar and stellar flares—and the synchrotron approximation breaks down, a few more approximations have been suggested. The simplest one is the analytical Dulk & Marsh (1982) approximation derived for isotropic power-law energy electron distributions, for a limited range of harmonic numbers

(20–100) and moderate viewing angles ( $30^\circ$ – $80^\circ$ ) relative to the magnetic field; no thermal plasma effect is included (Dulk 1985). In this range, the accuracy of these analytical formulae is within a few dozens of percent. Although this approximation can be used for rough estimates and parametric dependences, it is apparently insufficient for quantitative treatment or detailed modeling.

A better (fast numerical) approximation was proposed by Petrosian (1981) to calculate GS radiation ignoring the plasma and then generalized by Klein (1987) to include the plasma effect. This (Petrosian–Klein, PK) approximation is valid for a broader range of parameters and yields typically an accurate radiation intensity, although it is not so precise in polarization and it does not reproduce the GS harmonic structure at low frequencies, where it can often be important. The most severe limitation of the PK approximation is that it is only valid for isotropic (and weakly anisotropic) angular distributions of the emitting electrons.

However, there is currently ample evidence of anisotropic electron distributions in many cases, for example, in microwave bursts accompanying solar flares (Lee & Gary 2000; Melnikov et al. 2002; Fleishman et al. 2003; Altyntsev et al. 2008). The only way of calculating a GS radiation from the anisotropic distributions is currently through the use of exact formulae (Fleishman & Melnikov 2003a), which makes both the detailed GS modeling and, especially, forward fitting inversions (Altyntsev et al. 2008; Fleishman et al. 2009) prohibitively slow. This calls for the development of new, computationally effective schemes of the GS calculations taking into account the anisotropy (Fleishman et al. 2009).

This paper describes new approximate GS codes we developed for both isotropic and anisotropic electron distributions. To derive these codes we critically re-evaluated the assumptions made to obtain the PK approximation (and improved upon those assumptions where needed). These new codes allow for a large flexibility in selection of the computational options; e.g., they

can be optimized for accuracy or computation speed with the full range of the intermediate options between these two extremes. The code mode, which is precise for most practical applications, is two to three orders of magnitude faster than the exact code; the mode fully optimized for speed is even about one more order of magnitude faster. No competing approximate GS code is currently available for the anisotropic electron distributions; for the isotropic distributions, our code provides better accuracy than the PK code with a comparable computation speed.

## 2. METHODOLOGY

### 2.1. Exact GS Equations

Exact equations for the GS emissivity and absorption coefficient for an eigenmode  $\sigma$  in a magnetized plasma have the form (Eidman 1958, 1959; Melrose 1968; Ramaty 1969)

$$j_f^\sigma = \frac{2\pi e^2}{c} \frac{n_\sigma f^2}{1 + T_\sigma^2} \sum_{s=-\infty}^{\infty} \int \left[ \frac{T_\sigma(\cos \theta - n_\sigma \beta \mu) + L_\sigma \sin \theta}{n_\sigma \sin \theta} J_s(\lambda) + J'_s(\lambda) \beta \sqrt{1 - \mu^2} \right]^2 F(\mathbf{p}) \delta \left[ f(1 - n_\sigma \beta \mu \cos \theta) - \frac{sf_{\text{Be}}}{\gamma} \right] d^3 \mathbf{p}, \quad (1a)$$

$$\chi^\sigma = - \frac{2\pi e^2}{n_\sigma(1 + T_\sigma^2)} \sum_{s=-\infty}^{\infty} \int \left[ \frac{T_\sigma(\cos \theta - n_\sigma \beta \mu) + L_\sigma \sin \theta}{n_\sigma \sin \theta} J_s(\lambda) + J'_s(\lambda) \beta \sqrt{1 - \mu^2} \right]^2 \frac{1}{\beta} \left[ \frac{\partial F(\mathbf{p})}{\partial p} + \frac{n_\sigma \beta \cos \theta - \mu}{p} \frac{\partial F(\mathbf{p})}{\partial \mu} \right] \times \delta \left[ f(1 - n_\sigma \beta \mu \cos \theta) - \frac{sf_{\text{Be}}}{\gamma} \right] d^3 \mathbf{p}, \quad (1b)$$

where  $f$  is the emitting frequency,  $f_{\text{Be}} = eB/(2\pi m_e c)$  is the electron gyrofrequency,  $e$  and  $m_e$  are the electron charge and mass, respectively,  $B$  is the magnetic field,  $c$  is the speed of light,  $n_\sigma$ ,  $T_\sigma$ , and  $L_\sigma$  are the refraction index, and transverse and longitudinal (relative to the wave vector) components of the polarization vector, respectively (see Appendix A),  $\theta$  is the angle between the wave vector and the magnetic field vector,  $p$  and  $\beta = v/c$  are the electron momentum and normalized (by  $c$ ) velocity, respectively,  $\mu = \cos \alpha$ ,  $\alpha$  is the electron pitch angle (i.e., the angle between the electron momentum and the magnetic field vector),  $\gamma = (1 - \beta^2)^{-1/2}$  is the Lorentz factor,  $J_s(\lambda)$  and  $J'_s(\lambda)$  are the Bessel function and its derivative over the argument  $\lambda$ , respectively:

$$\lambda = \frac{f}{f_{\text{Be}}} \gamma n_\sigma \beta \sin \theta \sqrt{1 - \mu^2}. \quad (2)$$

The electron distribution function  $F(\mathbf{p})$  is normalized as follows (we assume that it is azimuthally symmetric, which results in the factor  $2\pi$ ):

$$\int F(\mathbf{p}) d^3 \mathbf{p} = 2\pi \int_{p_1}^{p_2} p^2 dp \int_{-1}^1 F(p, \mu) d\mu = n_e, \quad (3)$$

where  $n_e$  is the number density of electrons having momentum between  $p_1$  and  $p_2$ .

As has been said, Equations (1a) and (1b) are computationally expensive, so only a very limited number of studies utilizing the exact GS formulae for anisotropic electron distributions (see, e.g., Fleishman & Melnikov 2003a, 2003b; Fleishman 2006;

Altyntsev et al. 2008; Tzatzakis et al. 2008; Reznikova et al. 2009) have been performed. Most of the GS studies, therefore, were performed for the isotropic electron distributions, although the number of three-dimensional models considering either isotropic (Preka-Papadema & Alissandrakis 1992; Bastian et al. 1998; Fleishman et al. 2009) or anisotropic (Tzatzakis et al. 2008) electron distributions is still very limited.

The main reason for this lack of analysis is a long time required to compute the exact GS emissivity and absorption coefficient whose multiple calculations are needed to build a realistic three-dimensional model. For example, in a recently developed “GS Simulator” (Fleishman et al. 2009), which is capable of modeling GS emission from a predefined magnetic structure populated with a thermal plasma and accelerated electrons, the user currently can select between a fast PK code which is valid for the isotropic distributions only and a slow exact code which is correct for arbitrary anisotropic distribution. However, while using the PK code yields the full model output over a few minutes (of a standard PC CPU), the exact code requires a day or so to do a comparable simulation, which apparently restricts practical applications of this tool. Thus, there is a need for fast GS codes that are applicable for a broad range of isotropic and anisotropic distributions and plasma parameter combinations.

### 2.2. Petrosian–Klein Approximation for the Isotropic Case

The most successful algorithm available now for fast and reasonably precise computation of the GS radiation was proposed by Petrosian (1981) and then developed by Klein (1987). Below we consider the approximations adopted in the PK algorithm and then generalize them as needed to accommodate the anisotropic case and improve the overall accuracy of the output.

A key step of the PK algorithm is replacement of the summation over the discrete harmonic number  $s$  by integration over a corresponding continuous parameter

$$\sum_{s=-\infty}^{\infty} U(s) \simeq \int_{-\infty}^{\infty} U(s) ds, \quad (4)$$

which is formally valid if (1)  $|s| \gg 1$  and (2) the contributions of the adjacent terms,  $s$  and  $s + 1$ , are comparable, i.e.,  $U(s)$  changes smoothly for large  $s$ . Within the PK approximation, this replacement is adopted for all the harmonic numbers; then, the integral over  $s$  can easily be taken analytically using the  $\delta$ -function. Although replacement (4) is formally incorrect for low harmonic numbers and so the PK approximation cannot, in particular, reproduce a discrete (harmonic) structure of GS radiation at low frequencies, the approximate spectra do reproduce the mean level of the exact spectra remarkably well.

The mentioned replacement implies that in place of integer-order Bessel functions, real-order Bessel functions enter the integrals, whose numerical computation can be even more demanding than that of the integer-order Bessel functions. This calls for use of reliable fast approximations for the real-order Bessel functions. Klein (1987) points out that the approximate expressions for the Bessel functions and their derivatives proposed by Wild & Hill (1971) are applicable; so the use of the Wild & Hill (1971) expressions represents the second important assumption within the PK algorithm.

At this stage, the GS emissivity and absorption coefficient represent double integrals over  $dp$  and  $d\mu$ , which is still a computationally expensive task. The third key simplification

employed by Petrosian (1981) and Klein (1987) is the analytical Laplace estimation of the angular integral over  $d\mu$ . The Laplace integration method replaces the integrand by a best-fit Gaussian function and then analytically takes the integral of this Gaussian profile. Finding this Gaussian function requires one to determine the Gaussian peak  $\mu_0$  and width  $\Delta\mu_0$ . In a general case, the peak position  $\mu_0$  obeys an algebraic transcendental equation, although both Petrosian (1981) and Klein (1987) use a truncated simple analytical solution of this equation, the fourth approximation, which is approximately valid for the isotropic electron distributions, but insufficient to account for the pitch-angle anisotropy.

Finally, because the standard PK algorithm is not precise at low frequencies anyway, Klein (1987) adopts a fifth approximation—neglecting the longitudinal component of the eigenmode polarization vectors, which is indeed correct at high frequencies. Petrosian (1981) does not need this approximation since he considers the vacuum case, where no longitudinal wave component is present. Apparently, this approximation is minor and one can easily get rid of it by considering the full polarization vectors of the high-frequency eigenmodes in the magnetized plasma (see Appendix A).

### 2.3. Strategy of Petrosian–Klein Algorithm Generalization

To obtain a better approximation within the Petrosian (1981) and Klein (1987) guidelines we have to re-evaluate all five approximations described above in Section 2.2. In what follows we get rid of the fifth approximation and always use the full polarization vectors of the eigenmodes including the longitudinal component  $L_\sigma$ , see Equation (1). At the first stage of the generalization, we apply the replacement (4) for all harmonics to obtain a more precise analogy of the PK expressions valid for both isotropic and anisotropic electron distributions. In doing so, like in Klein (1987), we employ both integration over  $ds$  with the  $\delta$ -function and Wild & Hill (1971) approximate expressions for the Bessel functions. However, we more precisely evaluate the angular integral by more accurately fitting the corresponding integrand with a Gaussian. The output of this step yields “continuous” (i.e., without the discrete low-frequency harmonic structure) spectra, which are reasonably precise at high frequencies, while giving the correct mean level at low frequencies even when the harmonic structure is prominent in the exact expressions. This output is often even more precise for the anisotropic than for isotropic distributions and computationally comparably fast compared with the original Klein’s algorithm. We refer to this algorithm and this code as “continuous” ones.

At the second stage of the generalization, we improve the algorithm toward reproducing the harmonic structure at low frequencies. We tried a number of approaches to this problem and found that the best results are obtained when we use the exact (i.e., composed of summation over integer harmonics, in contrast to the “continuous” contribution discussed above) expressions at some low frequencies,  $f \leq f_{\text{cr}}^C$ , and apply the continuous approximation at higher frequencies; we refer to the corresponding output as the “hybrid” algorithm or the “hybrid” code.

At the third stage, we apply a number of optimizations to the continuous and hybrid algorithms. For example, for the discrete contribution we use the exact Bessel functions at low frequencies (where the use of the approximate expression was found to result in noticeable errors for some parameter combinations), typically at  $f/f_{\text{Be}} < 12$ , while we use the Wild & Hill (1971) approximations at higher frequencies. Also,

we introduce correcting multiplicative factors to ensure perfect matches at all matching frequencies, where we switch from exact to approximate Bessel functions or from the discrete to the continuous contribution. As a result, we obtain a gradually tunable algorithm of GS calculations, which is overall fast and precise, and whose precision can further be increased at the expense of computation speed, and vice versa. The fastest (the least precise) version of the code is still precise enough for most practical applications (except those specifically interested in the low-frequency harmonic structure of the GS emission), providing spectrum accuracy typically better than 5% and better than 10% for all studied parameter combinations within the code applicability range, see Section 3.3.

## 3. CONTINUOUS GS CODE

### 3.1. Analytical Derivation

Now we turn to the actual implementation of our generalization strategy starting with a more precise evaluation of the angular integrals. Making replacement (4) and performing integration over  $ds$  (using the  $\delta$ -function), we get

$$j_f \simeq \frac{4\pi^2 e^2}{c} \frac{nf^2}{f_{\text{Be}}(1+T^2)} \int_{p_1}^{p_2} \gamma p^2 dp \int_{-1}^1 \left[ \frac{T(\cos\theta - n\beta\mu) + L \sin\theta}{n \sin\theta} J_s(\lambda) + J'_s(\lambda)\beta\sqrt{1-\mu^2} \right]^2 F(p, \mu) d\mu, \quad (5a)$$

$$\varkappa \simeq -\frac{4\pi^2 e^2 m_e c}{n f_{\text{Be}}(1+T^2)} \int_{p_1}^{p_2} \gamma^2 dp \int_{-1}^1 \left[ \frac{T(\cos\theta - n\beta\mu) + L \sin\theta}{n \sin\theta} J_s(\lambda) + J'_s(\lambda)\beta\sqrt{1-\mu^2} \right]^2 \left[ p \frac{F'_p(p, \mu)}{F(p, \mu)} + (n\beta \cos\theta - \mu) \frac{F'_\mu(p, \mu)}{F(p, \mu)} \right] F(p, \mu) d\mu, \quad (5b)$$

where we omitted the wave-mode indices  $\sigma$  for brevity, and  $s$  is determined from the resonance condition and so has the form

$$s = \gamma \frac{f}{f_{\text{Be}}} (1 - n\beta\mu \cos\theta). \quad (6)$$

For electromagnetic waves  $n < 1$ , thus,  $s > 0$  and  $\lambda < s$ . Therefore, one can use the approximate expressions (Wild & Hill 1971; Klein 1987)

$$J_s(sx) \simeq \frac{1}{\sqrt{2\pi s}} \frac{Z^s(x)}{a(s, x)}, \quad (7a)$$

$$J'_s(sx) \simeq \frac{b(s, x)}{\sqrt{2\pi s}} \frac{Z^s(x)}{x}, \quad (7b)$$

where  $sx = \lambda$  and

$$Z(x) = \frac{x \exp(\sqrt{1-x^2})}{1 + \sqrt{1-x^2}}, \quad (8a)$$

$$a(s, x) = \left[ (1-x^2)^{3/2} + \frac{A}{s} \right]^{1/6}, \quad A = 0.503297, \quad (8b)$$

$$b(s, x) = \left[ (1-x^2)^{3/2} + \frac{B}{s} \right]^{1/6} \left( 1 - \frac{1}{5s^{2/3}} \right), \quad B = 1.193000. \quad (8c)$$

Taking into account Equation (6), parameter  $x$  takes the form

$$x = \frac{\lambda}{s} = \frac{n\beta \sin \theta \sqrt{1 - \mu^2}}{1 - n\beta \mu \cos \theta}. \quad (9)$$

Substitution of the above expressions into formulae (5) for the emissivity and absorption coefficient yields

$$j_f \simeq \frac{2\pi e^2}{c} \frac{f}{n(1 + T^2) \sin^2 \theta} \int_{p_1}^{p_2} p^2 dp \int_{-1}^1 F(p, \mu) Z^{2s} Q d\mu, \quad (10a)$$

$$\kappa \simeq -\frac{2\pi e^2 m_e c}{n^3 f (1 + T^2) \sin^2 \theta} \int_{p_1}^{p_2} \gamma dp \int_{-1}^1 F(p, \mu) Z^{2s} Q R d\mu, \quad (10b)$$

where

$$Q = \frac{[T(\cos \theta - n\beta \mu) + L \sin \theta + ab(1 - n\beta \mu \cos \theta)]^2}{a^2(1 - n\beta \mu \cos \theta)}, \quad (11)$$

$$R = p \frac{F'_p(p, \mu)}{F(p, \mu)} + (n\beta \cos \theta - \mu) \frac{F'_\mu(p, \mu)}{F(p, \mu)}. \quad (12)$$

As has been explained, following Petrosian (1981) and Klein (1987), we estimate the integral over  $d\mu$  in Equation (10) using the fastest descent (Laplace) method, which results in the following equations:

$$j_f \simeq \frac{2\pi e^2}{c} \frac{f}{n(1 + T^2) \sin^2 \theta} \int_{p_1}^{p_2} p^2 F(p, \mu_0) Z_0^{2s_0} Q_0 \sqrt{-\frac{2\pi}{h''(\mu_0)}} dp, \quad (13a)$$

$$\kappa \simeq -\frac{2\pi e^2 m_e c}{n^3 f (1 + T^2) \sin^2 \theta} \int_{p_1}^{p_2} \gamma F(p, \mu_0) Z_0^{2s_0} Q_0 R_0 \sqrt{-\frac{2\pi}{h''(\mu_0)}} dp, \quad (13b)$$

where index 0 means that the corresponding factor must be taken at the (yet to be calculated) value  $\mu_0 = \mu_0(p)$  at which the function  $h(p, \mu)$ ,

$$h = \ln[F(p, \mu) Z^{2s} Q] = \ln F(p, \mu) + 2s \ln Z + \ln Q, \quad (14)$$

reaches its peak value as a function of  $\mu$  for a given  $p$  value.

Petrosian (1981) and Klein (1987) justified applicability of the Laplace method by the fact that, for isotropic or weakly anisotropic distributions, the variation of the angular integrands in Equations (10a) and (10b) is dominated by the factor  $Z^{2s}$  whose dependence on  $\mu$  is very sharp (and very similar to a Gaussian, due to the nature of that factor, see Equation (8a)). Thus, one may use a Gaussian fit instead of the exact expression, and so Equations (13a) and (13b) are explicitly obtained by analytical integration of the corresponding Gaussian fits. However, validity of the above approximation for the anisotropic distributions in a general case is not that obvious and requires further analysis. Figure 1 displays a representative set of angular integrands in Equation (10a) for several pitch-angle distributions:

- (1) an Isotropic distribution;
- (2) a Gaussian distribution with the maximum at the pitch angle of  $90^\circ$

$$F(p, \mu) \sim \exp\left(-\frac{\mu^2}{\Delta\mu^2}\right) \quad (15)$$

with  $\Delta\mu = 0.1$ ; and

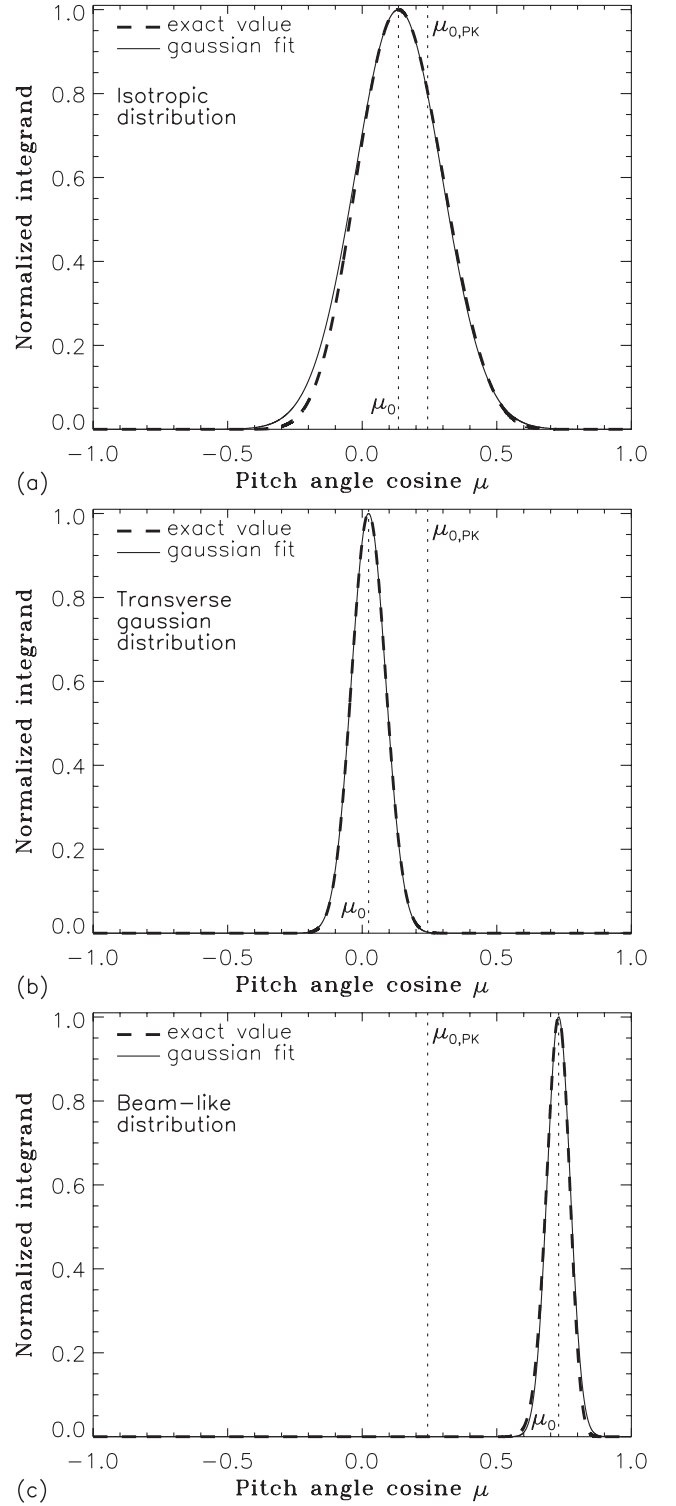


**Figure 1.** Angular integrand (normalized) in Equation (10a) for different electron distributions: (a) isotropic; (b) transverse Gaussian; and (c) beam-like Gaussian. The integrands themselves are shown by thick dashed lines, while solid lines are the corresponding Gaussian fits.

- (3) a beam-like distribution with the maximum at zero pitch angle

$$F(p, \mu) \sim \exp\left[-\frac{(\mu - 1)^2}{\Delta\mu^2}\right] \quad (16)$$

with  $\Delta\mu = 0.1$ .

The plots in Figure 1 correspond to the following parameters: X-mode, background plasma density  $n_0 = 5 \times 10^9 \text{ cm}^{-3}$ , magnetic field  $B = 270 \text{ G}$ , emission frequency  $f = 10 \text{ GHz}$ , emission direction  $\theta = 75^\circ$ , electron energy  $E = 1 \text{ MeV}$ ; the integrands are normalized to unity by their maximum values. Apparently, the Gaussian fits to the integrands are comparably good for both isotropic and anisotropic cases, which makes the Laplace method of angular integral evaluation widely applicable. Note that the used value of  $\Delta\mu = 0.1$  describes the case of rather strong anisotropy, which has a huge effect on the GS radiation.

For each momentum  $p$ , the peak position  $\mu_0$  is determined as the root of equation  $h'(\mu) = 0$ , where  $h'(\mu)$  is the derivative of function  $h(p, \mu)$  (Equation (14)) over  $\mu$ :

$$h'(\mu) = \frac{F'_\mu(p, \mu)}{F(p, \mu)} + 2\gamma \frac{f}{f_{\text{Be}}} \left[ \frac{n\beta \cos \theta - \mu}{1 - \mu^2} \sqrt{1 - x^2} - n\beta \cos \theta \ln Z \right] + (\ln Q)', \quad (17)$$

$$(\ln Q)' = 2 \frac{ab[(a'/a + b'/b)(1 - n\beta\mu \cos \theta) - n\beta\mu \cos \theta] - Tn\beta}{T(\cos \theta - n\beta\mu) + L \sin \theta + ab(1 - n\beta\mu \cos \theta)} - 2 \frac{a'}{a} + \frac{n\beta \cos \theta}{1 - n\beta\mu \cos \theta}, \quad (18a)$$

$$\frac{a'}{a} = \frac{\chi(A\eta - \xi)}{a^6}, \quad (18b)$$

$$\frac{b'}{b} = \frac{\chi(B\eta - \xi)}{b_1^6} + 4\chi n\beta \cos \theta \frac{b_2 - 1}{b_2}, \quad (18c)$$

$$b_1 = \left[ (1 - x^2)^{3/2} + \frac{B}{s} \right]^{1/6}, \quad b_2 = \left( 1 - \frac{1}{5s^{2/3}} \right), \quad b = b_1 b_2, \quad (18d)$$

$$\chi = \frac{\gamma f}{6s f_{\text{Be}}}, \quad \eta = \frac{n\beta \cos \theta}{s}, \quad \xi = 3x^2(n\beta \cos \theta - \mu) \frac{\sqrt{1 - x^2}}{1 - \mu^2}. \quad (18e)$$

Transcendental Equation (17) has no closed solution for  $\mu_0$  in a general case. For isotropic case, the derivative of the distribution function vanishes, and then discarding terms  $\ln Z$  and  $\ln Q$  from Equation (17) yields  $\mu_{0,\text{PK}} \approx n\beta \cos \theta$ , which is approximately valid for the isotropic case as shown in Figure 1(a). Petrosian (1981) and Klein (1987) applied this approximate root to derive their approximate GS codes. In the general case, however, when the pitch-angle anisotropy is not necessarily weak, this approximation breaks down. Inspection of Figure 1 suggests that the accuracy of the integral evaluation can be significantly improved if one uses the exact solution  $\mu_0$  of transcendental Equation (17) in place of the approximate one  $\mu_{0,\text{PK}}$ . Indeed, the solution of transcendental equations can easily be found numerically, e.g., with the bisection method (see, e.g., Press et al. 1997). The vertical dotted lines in Figure 1 show the position of the approximate root  $\mu_{0,\text{PK}}$  used in the PK algorithm. This approximate root noticeably deviates from the true solution even for the isotropic electron distribution; thus, in addition to accounting for the anisotropic distributions, using

the exact numeric solution for  $\mu_0$  also improves the accuracy of GS computation from the isotropic distributions.

The second derivative of  $h(p, \mu)$  over  $\mu$  has the form

$$h''(\mu) = \frac{F'_\mu(p, \mu)}{F(p, \mu)} - \left[ \frac{F''_{\mu\mu}(p, \mu)}{F(p, \mu)} \right]^2 - 2\gamma \frac{f}{f_{\text{Be}}} \frac{\sqrt{1 - x^2}}{1 - \mu^2} \times \left[ 1 + \frac{(n\beta \sin \theta)^2(n\beta \cos \theta - \mu)^2}{(1 - n\beta\mu \cos \theta)^3(1 - x^2)} - \frac{2\mu(n\beta \cos \theta - \mu)}{1 - \mu^2} + \frac{n\beta \cos \theta(n\beta \cos \theta - \mu)}{1 - n\beta\mu \cos \theta} \right] + (\ln Q)'''. \quad (19)$$

The analytical expression for the term  $(\ln Q)'''$  is very cumbersome. As a rule, the contribution of this term is minor. However, we found that for some combinations of parameters (including, e.g., isotropic distribution), the account of  $(\ln Q)'''$  noticeably increases the computation accuracy. In such cases, it is more convenient to calculate  $(\ln Q)'''$  by explicit numerical differentiation of  $(\ln Q)'$ , see Equation (18a).

Electron distributions  $G(E, \mu)$  over energy  $E$  (in place of momentum  $p$ ) are often used in GS calculations. One can easily adjust Equations (10)–(13) to this form of the distribution function by making a simple variable transformation to integration over energy  $E$ . The emissivity and absorption coefficient then take the form

$$j_f \simeq \frac{2\pi e^2}{c} \frac{f}{n(1 + T^2) \sin^2 \theta} \int_{E_1}^{E_2} dE \int_{-1}^1 Z^{2s} QG(E, \mu) d\mu \\ \simeq \frac{2\pi e^2}{c} \frac{f}{n(1 + T^2) \sin^2 \theta} \int_{E_1}^{E_2} Z_0^{2s_0} Q_0 G(E, \mu_0) \sqrt{-\frac{2\pi}{h''(\mu_0)}} dE, \quad (20a)$$

$$\kappa \simeq -\frac{2\pi e^2 c}{n^3 f (1 + T^2) \sin^2 \theta} \int_{E_1}^{E_2} dE \int_{-1}^1 Z^{2s} QR^{(E)} d\mu \\ \simeq -\frac{2\pi e^2 c}{n^3 f (1 + T^2) \sin^2 \theta} \int_{E_1}^{E_2} Z_0^{2s_0} Q_0 R_0^{(E)} \sqrt{-\frac{2\pi}{h''(\mu_0)}} dE, \quad (20b)$$

where

$$R^{(E)} = \frac{\partial G(E, \mu)}{\partial E} - \frac{1 + \beta^2}{cp\beta} G(E, \mu) + \frac{n\beta \cos \theta - \mu}{cp\beta} \frac{\partial G(E, \mu)}{\partial \mu} \quad (21)$$

and the distribution function  $G(E, \mu)$  is normalized as follows:

$$2\pi \int_{E_1}^{E_2} dE \int_{-1}^1 G(E, \mu) d\mu = n_e. \quad (22)$$

Then, the logarithmic derivatives of the function  $F(p, \mu)$  in Equations (17) and (19) must be replaced by the corresponding derivatives of the distribution function  $G(E, \mu)$ :

$$\frac{F'_\mu(p, \mu)}{F(p, \mu)} = \frac{G'_\mu(E, \mu)}{G(E, \mu)}, \quad \frac{F''_{\mu\mu}(p, \mu)}{F(p, \mu)} = \frac{G''_{\mu\mu}(E, \mu)}{G(E, \mu)} \quad (23)$$

at a given energy  $E$ .

### 3.2. Numeric Implementation

The described algorithm was implemented in two (basically identical) numeric source codes—in FORTRAN and C++. We adopted a factorized form of the distribution function

$$G(E, \mu) = u(E)g(\mu), \quad (24)$$

where the type of the factors can be selected from a predefined list of options, similar to those used typically in X-ray modeling and data analysis. For example, the distribution over energy  $u(E)$  can be a single or double power law over energy, momentum, or Lorentz factor, include a thermal component matched to a nonthermal tail (so-called thermal–nonthermal distribution, TNT; see Holman & Benka 1992; Benka & Holman 1994), or have a form of kappa distribution. The angular distribution can be a Gaussian or modified (with a fourth-order term in the exponent) Gaussian function, or a loss-cone distribution; an isotropic distribution ( $g(\mu) = \text{constant}$ ) is also a possibility. For the full list of the built-in energy and pitch-angle distributions, see Appendix B. For a factorized form, Equation (24), the logarithmic derivatives of  $G(E, \mu)$  are equal to the corresponding logarithmic derivatives of  $g(\mu)$ , so we made the replacements

$$\frac{G'_\mu(E, \mu)}{G(E, \mu)} = \frac{g'(\mu)}{g(\mu)}, \quad \frac{G''_{\mu\mu}(E, \mu)}{G(E, \mu)} = \frac{g''(\mu)}{g(\mu)}. \quad (25)$$

As has been explained, finding a precise solution for  $\mu_0$  is very important to ensure the highest accuracy of the Laplace estimate of the angular integral, which is in turn a key to providing the overall accuracy of the algorithm. This root is a solution of the transcendental equation  $h'(\mu) = 0$ . We found that this equation always has a unique solution if we discard the term  $(\ln Q)'$  from Equation (17), so a simple bisection method of the root finding can efficiently be used. This approximation typically yields a very good approximation of the exact  $\mu_0$  value, so the term  $(\ln Q)'$  is a small correction; however, its inclusion in the equation improves the accuracy of the algorithm for some parameter combinations, especially for  $O$ -mode radiation. A disadvantage of having this term in the equation is that the function  $h'(\mu)$  can become discontinuous (for some parameter combinations) and so the simple bisection method can converge to the discontinuity point instead of the true root. We found two equally good approaches to correctly account for the  $(\ln Q)'$  contribution. In the first of them, the bisection method is first used to find  $\mu_{00}$  when the term  $(\ln Q)'$  is discarded and a correction to it,  $\Delta\mu$ , is determined analytically by the perturbation theory:  $\Delta\mu = -(\ln Q(\mu_{00}))'/h''(\mu_{00})$ . Then, this correction is used to set up the restricted interval of  $\mu$  around  $\mu_{00}$  in which the true solution of the full equation  $h' = 0$  (i.e., with  $(\ln Q)'$  included) is being specified by the bisection method. In the second one, the approximate root  $\mu_{00}$  is also determined first and then it is improved with the secant method (Press et al. 1997). Both methods proved to give the same results with comparable computational expenses (the second one is marginally longer).

The last step of the numeric implementation is integration over energy/momentum with the adopted distribution function. Since we use a number of different distribution functions, we also use a few different methods of the numeric integration. For the thermal distribution and the thermal-like (low-energy) parts of the TNT and kappa distributions, we use a Gaussian integration or the trapezoidal method with equally spaced nodes. For the power-law distributions and the power-law-like (high-energy) tails of the TNT and kappa distributions, the trapezoidal

or extended midpoint methods with logarithmic node placement (which gives an exact solution for the true power-law integrand) are applied (Bastian 2006). We also used the trapezoidal integration method with step-by-step accuracy improvement (Romberg integration; Press et al. 1997). For all the methods, we tried to find an optimal balance between the accuracy and the computation speed, which was achieved by appropriate choice of either the number of nodes in the trapezoidal or extended midpoint methods or the desired accuracy in the Romberg method. In all cases, the codes also include the free–free contribution to the radiation, which is extremely fast to compute.

Figures 2–4 demonstrate a few representative examples of the GS spectra computed with (1) exact equations, (2) a discrete approximation, i.e., exact equations in which the approximate expressions of the Bessel functions (Wild & Hill 1971) are used in place of exact ones, and (3) our new continuous approximation. The spectra were obtained under the assumption of a homogeneous source located at the Sun, i.e., the emission intensity (observed at the Earth) of the magnetoionic mode  $\sigma$  was calculated using the formula

$$I_f^\sigma = \frac{S}{\mathcal{R}^2} \frac{j_f^\sigma}{\chi^\sigma} (1 - e^{-\chi_\sigma L}), \quad (26)$$

where  $S$  and  $L$  are the visible source area and its depth along the line-of-sight, respectively, and  $\mathcal{R} \simeq 1.49 \times 10^{13}$  cm is the astronomical unit. Total emission intensity equals  $I_f = I_f^X + I_f^O$ , and the degree of polarization is defined as

$$\eta = \frac{I_f^X - I_f^O}{I_f^X + I_f^O}. \quad (27)$$

The plots in Figures 2–4 correspond to the following parameters: background plasma density  $n_0 = 2 \times 10^9$  cm $^{-3}$  and temperature  $T_0 = 4$  MK, magnetic field  $B = 370$  G, accelerated electrons have a power-law energy spectrum  $F \sim E^{-\delta}$  with  $\delta = 3.5$  between  $E_{\min} = 0.01$  MeV and  $E_{\max} = 10$  MeV, the number density of fast electrons  $n_b = 9.3 \times 10^7$  cm $^{-3}$ , visible source area  $S = 1.8 \times 10^{18}$  cm $^2$ , and source depth  $L = 6 \times 10^8$  cm. In Figure 2, the electron pitch-angle distribution is isotropic and the emission direction  $\theta = 30^\circ$ . In Figure 3, the electrons have a loss-cone distribution (Equation (15)) with  $\Delta\mu = 0.2$  and  $\theta = 60^\circ$ . In Figure 4, the electrons have a beam-like distribution (Equation (16)) with  $\Delta\mu = 0.2$  and  $\theta = 60^\circ$ . The integrals and series in the exact and approximate discrete expressions were calculated with relative accuracy  $10^{-5}$ .

Very high overall accuracy of radiation intensity, degree of polarization, and spectral index of the new approximation is evident, especially at high frequencies, where the slope of the true spectrum is reproduced well in all considered cases. In some cases, however, a small systematic offset of the continuous approximation relative to the exact one is noticeable, which is partly related to the use of approximate Bessel function expressions (note the corresponding offsets between the exact and approximate discrete curves). Thus, using a better approximation for the Bessel functions can further improve the accuracy of our continuous approximation. At low frequencies, the continuous approximation is intrinsically unable to reproduce the harmonic structure of the GS emission, although the mean level of the spectra is reproduced remarkably well. Due to the same reasons, the continuous approximation cannot account for the cyclotron maser instability (the negative absorption coefficient  $\chi_\sigma$  which results in coherent wave amplification). This instability can occur if the emission frequency is close to low harmonics

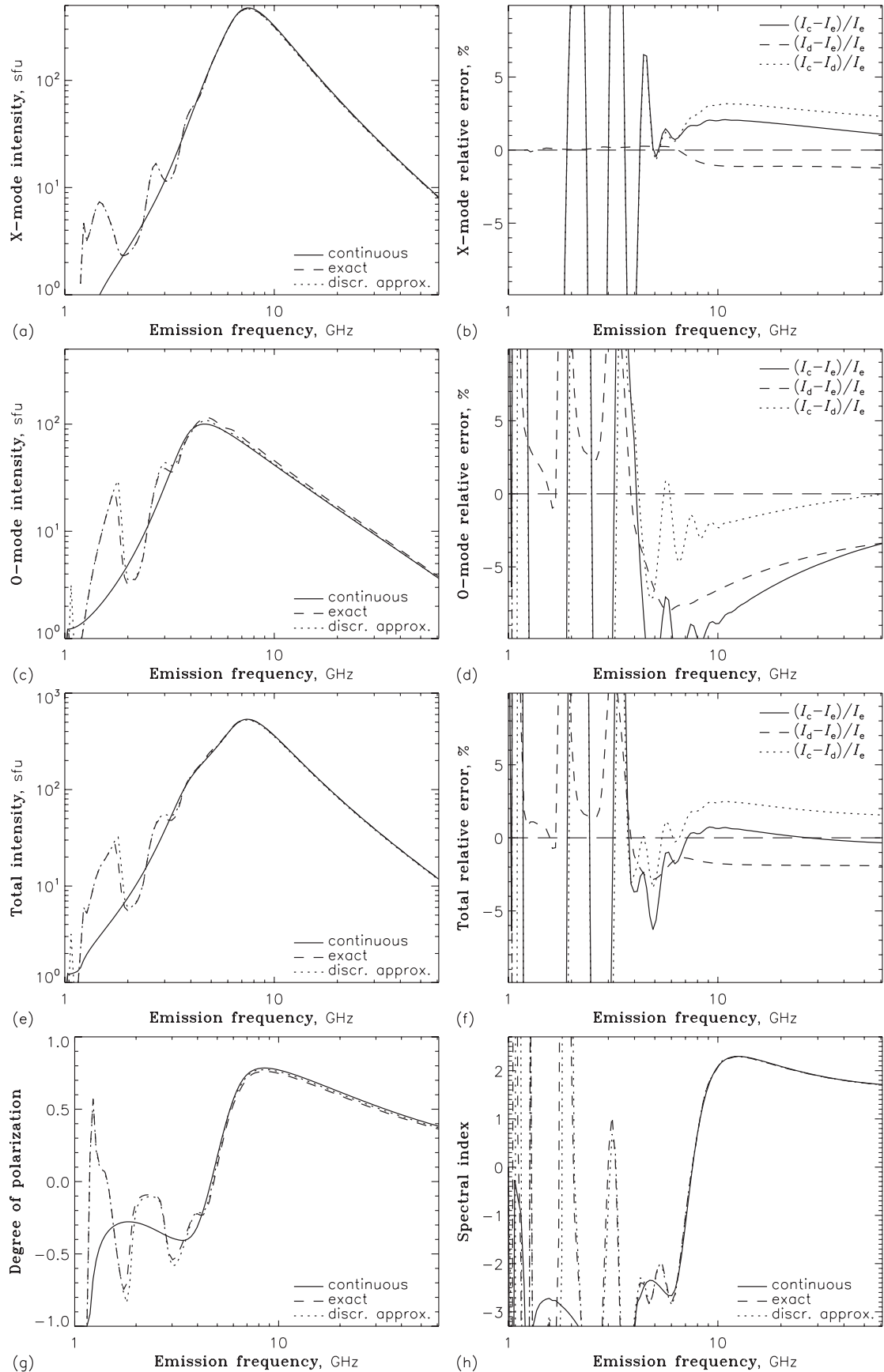


**Figure 2.** Calculated parameters of the GS emission for the isotropic electron distribution; adopted parameters are given in the text.

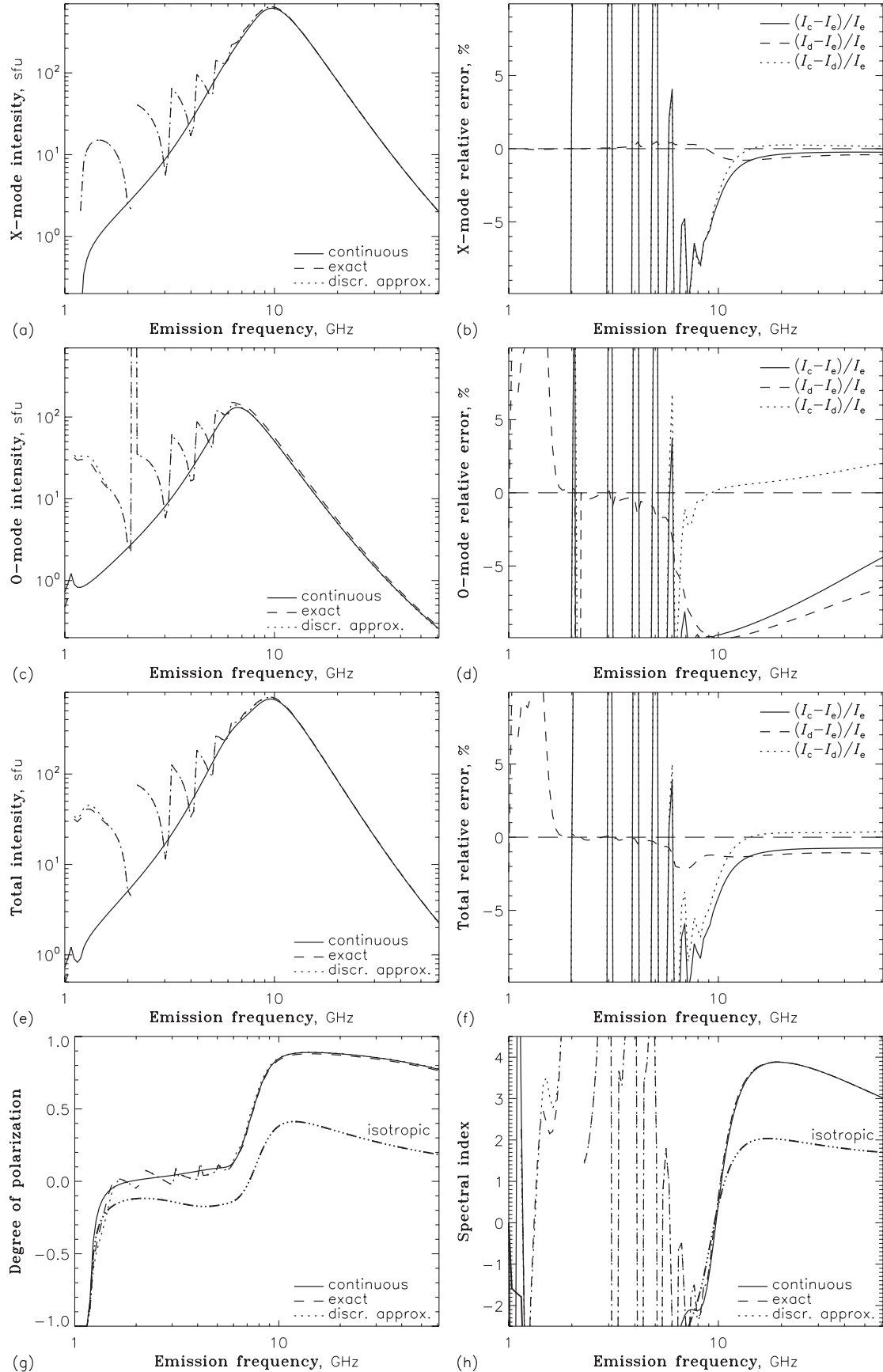


**Figure 3.** Calculated parameters of the GS emission for the transverse Gaussian electron angular distribution. In the two lower panels, the dash-triple-dotted line shows the corresponding parameters for the isotropic distribution calculated using the continuous code.

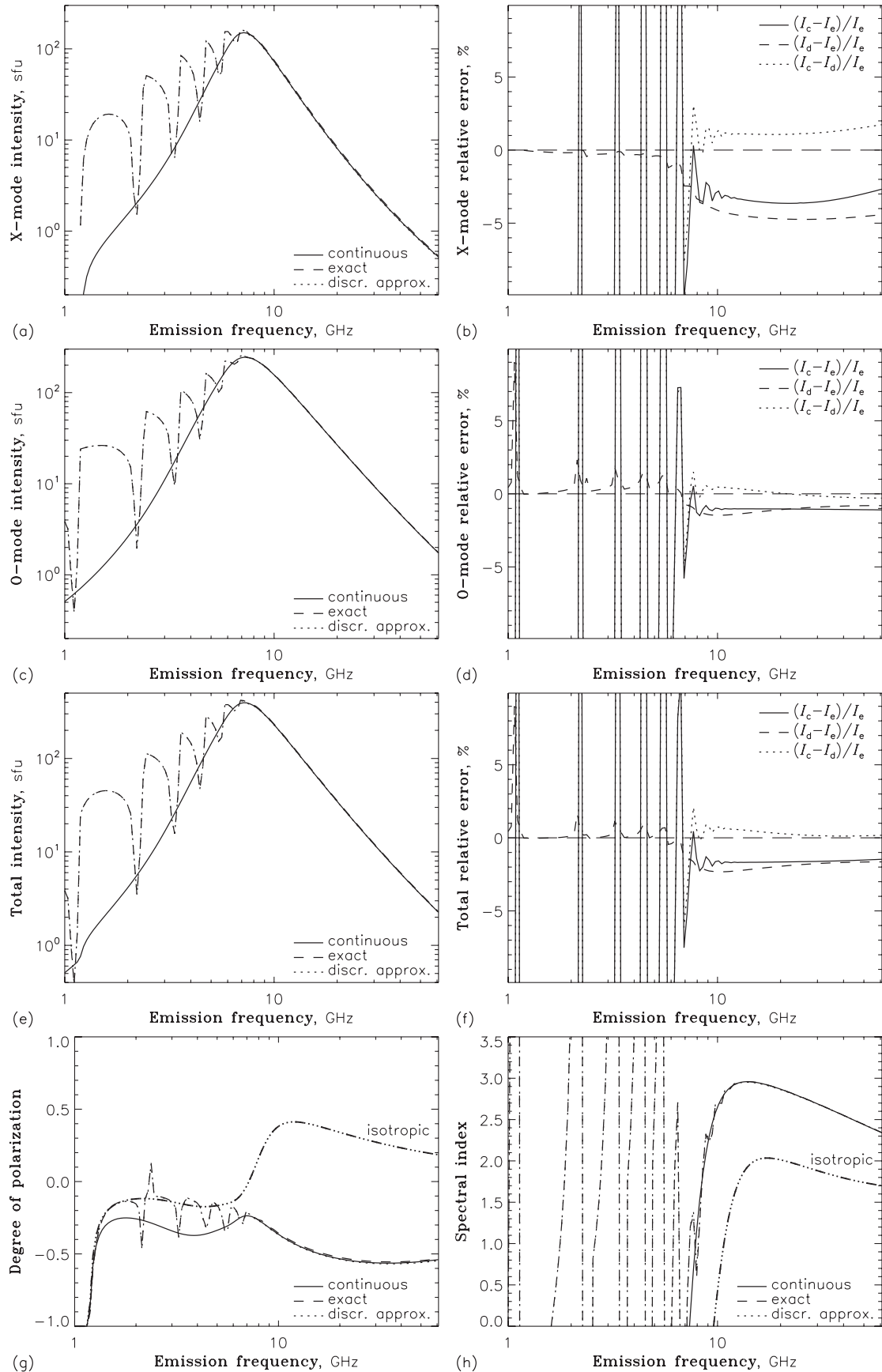


**Figure 4.** Calculated parameters of the GS emission for the beam-like electron distribution. In the two lower panels, the dash-triple-dotted line shows the corresponding parameters for the isotropic distribution calculated using the continuous code.

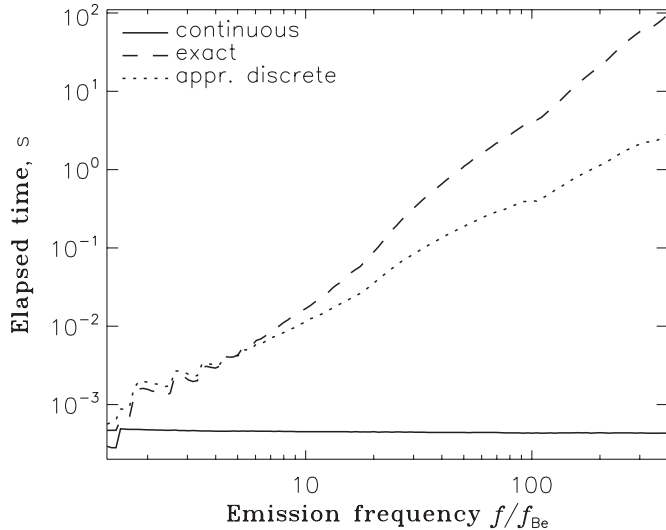


**Figure 5.** Time required to calculate the intensity and polarization of the GS emission (that is, the parameters  $j_f^X$ ,  $j_f^O$ ,  $\chi^X$ , and  $\chi^O$ ) at a given frequency. The simulation parameters are the same as in Figure 3. A 2 GHz Intel Pentium processor was used for the calculations.

of the cyclotron frequency, and typically requires an anisotropic electron distribution with  $R > 0$ , where  $R$  is specified by Equation (12). One can see an example of the maser instability in Figure 3(c) (loss-cone electron distribution,  $O$ -mode): the graphs for the exact equations and the discrete approximation have a very sharp peak at  $f \simeq 2f_{\text{Be}}$  (2 GHz) while the continuous approximation misses this feature.

We emphasize that the continuous approximation works equally well for both the isotropic distribution and for anisotropic distributions having a strong effect on GS emission, which we refer to as “strong anisotropy” in this context. To show this explicitly, we added the degree of polarization and spectral index curves corresponding to the case of isotropic electron distribution (all other simulation parameters being the same as for the anisotropic distributions) in Figures 3(g) and (h) and Figures 4(g) and (h). One can see that the anisotropy affects both the spectral index and the degree of polarization quite significantly; in particular, for the beam-like distribution, the polarization even changes its sign compared to the isotropic case. This explicitly confirms quantitative applicability of our continuous codes to strongly anisotropic electron distributions.

We performed all possible measures to optimize our codes, and the programs written in FORTRAN and C++ are checked to be comparably fast for comparable numeric settings. The continuous codes are much faster than the exact algorithm implementations. Figure 5 displays how the computation speed changes with the emission frequency (that, in turn, determines the maximal harmonic number used in the computations). For both exact and approximate discrete implementations, the computation time increases nearly exponentially with the harmonic number, while for the continuous approximation this time does not depend on the harmonic number at all. Thus, the achieved improvement in the computation speed is remarkably great.

### 3.3. Applicability Region of the Continuous Code

Perhaps no approximation can entirely substitute its exact prototype for all possible parameter combinations; thus, we specifically looked for those cases when the accuracy of the continuous codes decreases noticeably. As has been shown

(see Figure 1), the basic reason of the overall success of the approximation is the possibility to precisely fit the angular integrand by a Gaussian whose parameters are determined based on analytical properties of the integrand. Therefore, we can expect that the code performance will drop when the integrand cannot be fitted well by a Gaussian profile, for example, when the integrand is essentially asymmetric.

We found that for all analytical functions (continuous functions with all continuous derivatives) the approximation works well regardless of the function sharpness. However, if the angular distribution function or its first derivative have a discontinuity at a certain  $\alpha_c$ , then the angular integrand cannot be precisely fitted by a Gaussian for some range of the emission angle  $\theta$  around the angle  $\alpha_c$  and the accuracy of the GS spectrum computation drops noticeably here: the approximate intensity can differ from the exact one by up to a factor of two.

Such behavior of the approximate algorithm is in fact expected for the discontinuous angular electron distributions. We point out that even for an angular distribution function with a discontinuity of the second derivative at some  $\alpha_c$ , the accuracy of the continuous code can decrease around  $\theta \simeq \alpha_c$ . As an example, we consider a Gaussian loss-cone distribution  $g(\mu) = \text{constant}$  for  $\mu \leq \cos \alpha_c$ , and  $g(\mu) \sim \exp[-(\mu - \cos \alpha_c)^2 / \Delta\mu^2]$  for  $\mu > \cos \alpha_c$ , whose second derivative has a discontinuity at  $\alpha_c$ , while the first derivative and the function itself are both continuous.

Figures 6 and 7 display an example of when the angular integrand becomes noticeably asymmetric around the loss-cone boundary  $\alpha_c$  and the Gaussian function fails to provide a good fit to the integrand. This happens, however, only when the distribution function decreases very fast at  $\mu > \cos \alpha_c$ ; in the given example, we use  $\alpha_c = 80^\circ$  and  $\Delta\mu = 0.05$  (viewing angle  $\theta = 80^\circ$ , other simulation parameters are the same as in Figure 3, and the integrands in Figure 6 are plotted for the electron energy  $E = 1$  MeV). One can see that the angular integrand deviates from a Gaussian for both the  $X$ - and the  $O$ -modes; however, the integrand asymmetry is more significant for the  $O$ -mode. As a result, the continuous code fails to precisely reproduce the emission intensity, and the error is larger for the  $O$ -mode. We found that for smoother angular gradients,  $\Delta\mu \geq 0.1$ , which are still sharp enough for most practical applications, the integrand asymmetry remains small and the algorithm works well.

We conclude that although the algorithm can fail for some models of the angular distribution, it has to work well for any natural distribution function since it (being a solution of a transport equation) is supposed to be an analytical function continuous with all the derivatives.

## 4. HYBRID GS CODES

Although the continuous approximation is sufficient for many practical applications, the low-frequency harmonic structure can also often be of interest, especially for the anisotropic case (Fleishman & Melnikov 2003b). Therefore, in this section we describe a number of improvements of the code toward recovery of the harmonic structure and overall higher accuracy of the codes.

### 4.1. Harmonic Structure Recovery

We tried a few approaches to recover the GS harmonic structure at low frequencies and found that the simplest and most straightforward approach ensures the best results. In fact, to recover the harmonic structure at frequencies  $f < f_{\text{cr}}^C$  it

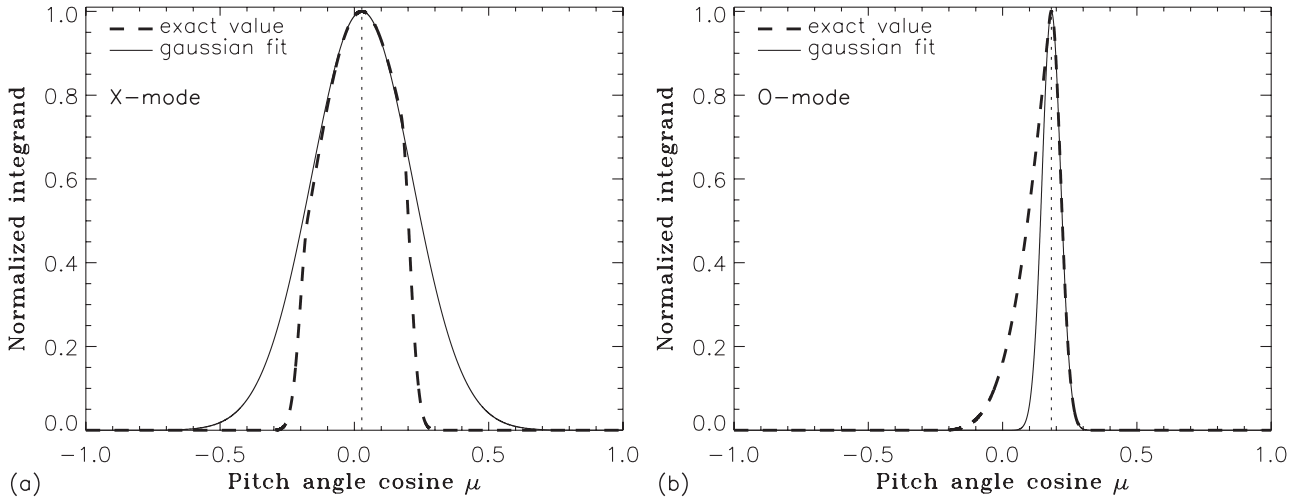


**Figure 6.** Angular integrand (normalized) in Equation (10a) for the loss-cone distribution with  $\alpha_c = 80^\circ$  and  $\Delta\mu = 0.05$  (for the X- and O-modes).

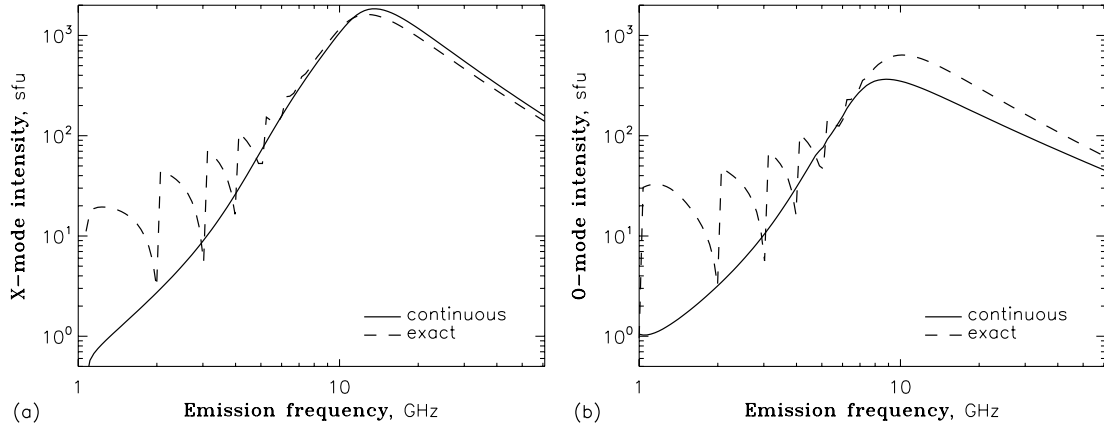


**Figure 7.** Calculated spectrum for the least favorable parameter combination of GS emission (X- and O-modes) for the loss-cone distribution with the discontinuous second angular derivative of the distribution function.

is sufficient to use exact equations at  $f < f_{\text{cr}}^C$ , while the continuous approximation is used at higher frequencies. Since at low harmonics the computation speeds of both the exact and the approximate discrete codes are almost identical (Figure 5), while the error related to the use of the approximate Bessel function expression is the biggest at these frequencies, we use the exact code (with exact Bessel functions) at low frequencies.

Our numeric experiments show that for full recovery of noticeable low-frequency harmonics it is typically sufficient to use the exact code at  $f < f_{\text{cr}}^C$  with  $f_{\text{cr}}^C \simeq 12f_{\text{Be}}$  and the continuous codes above. From Figures 2–4 we know that at high frequencies the continuous contribution displays the same slope as the exact one, although the approximate spectrum can systematically be shifted by a small value relative to the exact spectrum. Thus, a simple transition from the exact contribution to the continuous one results in a matching jump or matching residual. To remove this jump, we renormalize the continuous contribution as follows. First, we find the ratio of the values calculated by the exact and approximate formulae at  $f = f_{\text{cr}}^C$ , and then we apply this factor to all values calculated for  $f > f_{\text{cr}}^C$  with the approximate code, i.e.,

$$j_f^\sigma(f) = j_f^{\sigma C}(f) \frac{j_f^{\sigma E}(f_{\text{cr}}^C)}{j_f^{\sigma C}(f_{\text{cr}}^C)}, \quad \kappa^\sigma(f) = \kappa^{\sigma C}(f) \frac{\kappa^{\sigma E}(f_{\text{cr}}^C)}{\kappa^{\sigma C}(f_{\text{cr}}^C)}, \quad \text{for } f \geq f_{\text{cr}}^C, \quad (28)$$

where the upper indices E and C denote the values obtained using the exact and continuous codes, respectively. This renormalization provides a smooth transition from the exact to continuous contribution and also improves the accuracy of the spectra calculated at the high frequencies.

Since this code involves both exact and continuous contributions, we call it the “hybrid” code. With the matching frequency as an adjustable parameter of the code, the full range of options from a purely continuous code (if  $f_{\text{cr}}^C = 0$ ) to the exact code (if  $f_{\text{cr}}^C = \infty$  or very large) is available.

#### 4.2. Optimization of the Hybrid Code

For the vast majority of applications, the hybrid code with  $f_{\text{cr}}^C \leq 15f_{\text{Be}}$  or even the purely continuous code seems to be sufficient. Nevertheless, some problems or settings requiring even more precise computations can exist in some cases (for example, various testing problems). For such cases, we further optimize the code as follows. If  $f_{\text{cr}}^C \gg 10f_{\text{Be}}$  is needed, the use of the exact Bessel functions becomes more and more computationally demanding. We found that we can significantly increase the computation speed if we use the Wild & Hill (1971) expressions for the Bessel functions, and so the discrete approximation in place of the exact equations, at  $f > f_{\text{cr}}^{\text{WH}}$  with  $f_{\text{cr}}^{\text{WH}} \sim 10f_{\text{Be}}$ ; we use  $f_{\text{cr}}^{\text{WH}} = 12f_{\text{Be}}$  as a default value.

Apparently, the transition from the exact algorithm to the discrete approximation results in a matching residual at  $f = f_{\text{cr}}^{\text{WH}}$ ,

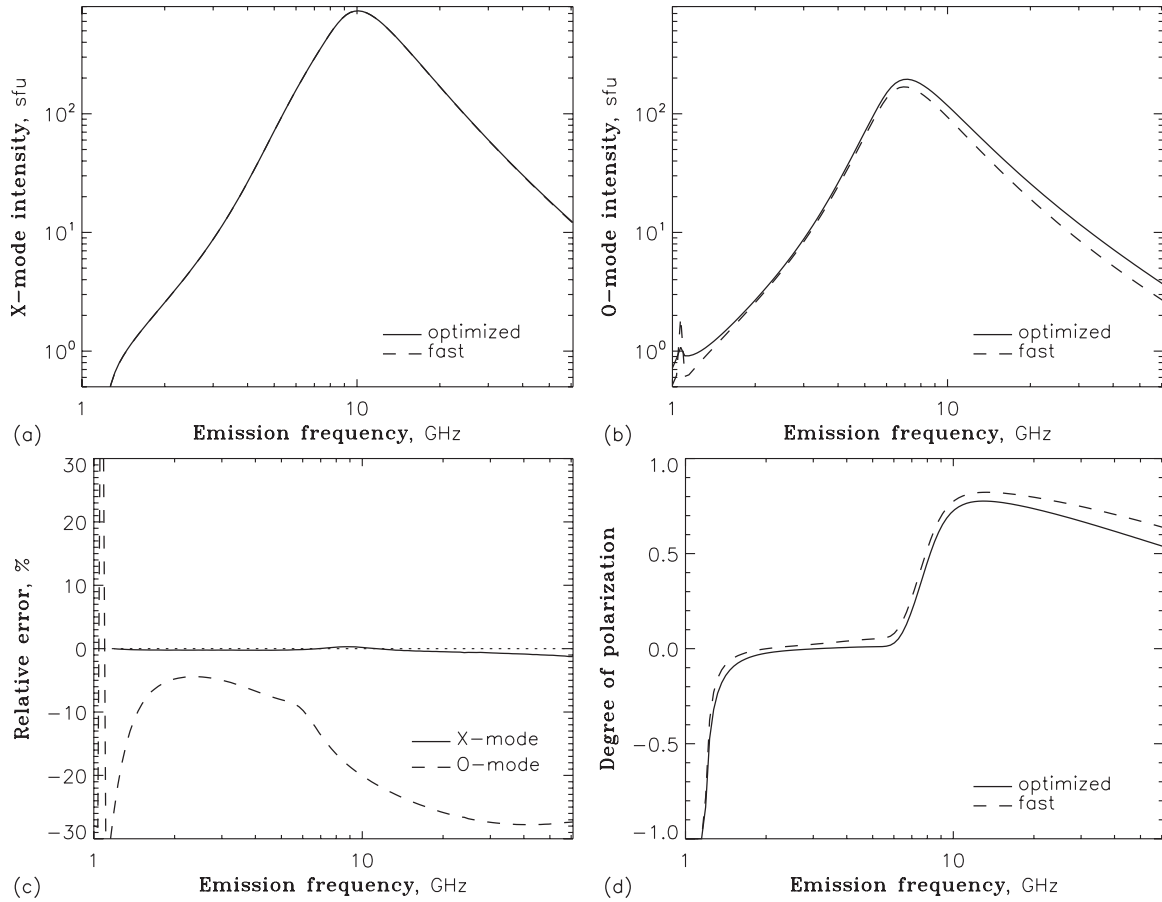


**Figure 8.** GS emission for the transverse Gaussian electron distribution calculated using different variants of the continuous code.

which is removed by the same renormalization as the one described in Section 4.1. As the frequency increases and reaches the next matching frequency  $f_{\text{cr}}^C$  (if indeed  $f_{\text{cr}}^C > f_{\text{cr}}^{\text{WH}}$ ), the discrete approximation gives way to the continuous approximation. This additional matching residual is removed by the same renormalization as before. Apparently, if  $f_{\text{cr}}^C \leq f_{\text{cr}}^{\text{WH}}$  then the discrete approximation is not applied, and so no additional renormalization is needed.

#### 4.3. Optimization of the Continuous Code

To round up the list of options and optimizations, we discuss a number of different versions of the continuous code. First of all, if we neglect the  $(\ln Q)'$  and  $(\ln Q)''$  terms in Equations (17) and (19), respectively, we obtain the code fully optimized for the computation speed. This code version produces the full GS spectrum at 100 frequencies and computes the degree of polarization in 15–30 ms depending on input distribution functions and the parameter combination. Typically, this version of the code produces spectra within the error better than 10%. The effect of neglecting the  $(\ln Q)'$  and  $(\ln Q)''$  is illustrated in Figure 8, where “optimized” and “fast” refer to the codes with and without the mentioned terms, respectively (the electrons are assumed to have a loss-cone distribution with  $\Delta\mu = 0.3$  and the other parameters are the same as in Figure 3).

Including the terms  $(\ln Q)'$  and  $(\ln Q)''$  reduces the error by a factor of two to the values better than 5% at the expense of increasing the computation time by around 70%. In many cases, this code yields highly precise spectra (error smaller than 2%–3%) at those frequencies where no harmonic structure is

pronounced. Nevertheless, we implemented one more optimization, which further improves the accuracy, when the code with  $(\ln Q)'$  and  $(\ln Q)''$  is not perfectly precise (the error is about 3%–5%). The idea behind this improvement is very simple: the entire spectrum is still calculated with the approximate continuous algorithm, while the exact calculations are performed at a single frequency (we found that the case with  $f = 12f_{\text{Be}}$  works well). Then, the continuous spectrum is renormalized as a whole to match the exact spectrum at this single frequency. This renormalization can reduce the errors of the continuous approximation by a factor of two or even better.

#### 4.4. Nomenclature of the Codes

Since we have developed and described many versions of the GS code, it is reasonable to summarize and compare them all, which is done in Table 1. The codes are ordered according to increasing computation time. The fastest code is the continuous code (C) which typically provides appropriate accuracy but does not reproduce the low-frequency harmonic structure. The optimized continuous codes (those with either  $(\ln Q)$ ,  $Q$ -optimized, and/or renormalization,  $R$ -optimized), which are basically the same continuous code but with better normalization, are only slightly slower and overall more precise than the continuous code (in particular, the polarization accuracy is improved greatly). No harmonic structure is reproduced either.

The hybrid codes (H) being composed of exact and/or approximate discrete contributions at low frequencies and of continuous contribution at high frequencies recover the harmonic structure. The first of them, the hybrid code, uses one matching

**Table 1**  
Summary of the GS Codes

Code Title	Approx. Used <sup>a</sup>	Rel. Time	Accuracy
Continuous	$ds$ , WH, LI, $\ln Q$	1	<5%–10%, no harmonics
$Q$ -optimized continuous <sup>b</sup>	$ds$ , WH, LI	1.6–1.8	<3%–5%, no harmonics
$R$ -optimized continuous <sup>b</sup>	$ds$ , WH, LI, $\ln Q$	2.0–2.5	<3%–5%, no harmonics
Optimized hybrid <sup>c</sup>	No/WH / $ds$ , WH, LI <sup>d</sup>	$\gtrsim 10^e$	Exact/as exact/< 2%–4%
Hybrid <sup>c</sup>	No/ $ds$ , WH, LI <sup>d</sup>	$\gtrsim 10^e$	Exact/<2%–4%
Approximate discrete	WH	Long	As exact at $f \gtrsim 10f_{Be}$
Exact	No	Longest	Exact

#### Notes.

<sup>a</sup> The following approximations can be used: “ $ds$ ”, integration over harmonics instead of summation; “WH”, approximated Bessel functions; “LI”, Laplace integration; “ $\ln Q$ ”, the terms  $(\ln Q)'$  and  $(\ln Q)''$  are neglected.

<sup>b</sup>  $R$ -optimization and  $Q$ -optimization can be applied simultaneously which increases both the accuracy and the computation time.

<sup>c</sup> In these codes, different approximations are applied at different emission frequencies.

<sup>d</sup> In the continuous (high-frequency) part of the spectrum, one can choose to neglect the derivatives of  $\ln Q$  as well. However, this creates only a minor increase in the computation speed while decreasing the accuracy.

<sup>e</sup> This speed estimation was made for  $f_{cr}^C = 12f_{Be}$ . With an increase of  $f_{cr}^C$ , the computation time for the optimized hybrid and hybrid codes increases and approaches the computation time for the approximate discrete and exact codes, respectively.

frequency for transition from the exact to continuous code. This version of the code is very practical as it is both fast (only about five times slower than the continuous code) and highly precise if one selects  $f_{cr}^C \sim 12f_{Be}$ . However, this code is much slower for  $f_{cr}^C \gg 10f_{Be}$ , which makes it impractical for such settings. The optimized hybrid code, which uses the exact algorithm at  $f < 12f_{Be}$ , while the discrete approximation between  $f_{cr}^{WH} = 12f_{Be}$  and  $f_{cr}^C > f_{cr}^{WH}$  allows one to increase the frequency  $f_{cr}^C$  with less computational expenses still providing very high accuracy. However, an increase of the computation time with  $f_{cr}^C$  is noticeable in this code as well (see Figure 5).

The approximate discrete code (D) uses the exact GS equations with only one approximation—the approximate Bessel function expressions are used. This approximation basically yields very accurate results (with some exceptions at low frequencies and sometimes a small systematic offset of the optically thin part of the  $O$ -mode spectrum). However, since the summation over the harmonics is performed for an arbitrary high frequency in this version of the GS code, the computation time can be orders of magnitude longer than for the hybrid and continuous codes. Finally, the exact code (E) uses no approximation and so it is capable of producing results with arbitrarily high precision at the expense of the computation time, which can become much longer than for the approximate discrete code because the time required to compute the exact Bessel function  $J_s$  increases with its order  $s$ . Overall, this set of the code implementations offers a complete list of options between the fast and accurate continuous code through slower and more precise hybrid codes to the discrete and exact codes with approximate or exact Bessel functions, respectively, so each potential user of the codes can make his or her own selection of the code option depending on the problem being studied.

## 5. CODE ACCESSIBILITY AND APPLICATION

To ensure the widest practical application of these new codes including the perspective users who work more with IDL than with the computing languages like FORTRAN and C++, the above described codes were implemented as Windows dynamic link libraries (DLLs) and Linux shared objects (SOs) callable from IDL. A brief description<sup>q</sup> of these libraries is

given in Appendix B. The libraries themselves with complete descriptions (including the calling sequence, input and output parameters, keys to switch between the different code versions, and the built-in distribution functions), examples of the calling IDL programs, and sample outputs are available in the online version of the journal.

Although our GS codes can be used for various astrophysical objects (e.g., active stars, planetary magnetospheres, cosmic jets) and even for laboratory settings, we have been developing them with solar flares in mind as the primary target. In particular, this is why the calculated emission intensity is normalized to the distance from the Sun to the Earth. The supplementary material in the online version of the journal contains a few sample spectra employing parameters typical for solar flares.

Here, we illustrate how the code application can be used to address key physics of solar flares. We note that using oversimplified approximate GS expressions has often led to a conclusion that the number of accelerated electrons deduced from hard X-ray (HXR) observations was insufficient to produce the observed microwave emission with a difference of up to two to three orders of magnitude. Although the simulations using exact GS expressions (e.g., Altintsev et al. 2008) do not confirm that conclusion, the use of the exact codes is highly time-consuming and so impractical.

Let us specifically consider an occulted solar flare of 2007 December 31 recently reported by Krucker et al. (2010). This flare is particularly interesting because Krucker et al. (2010) argued that the observed coronal HXR source represented the very acceleration site of the flare; probing the acceleration regions is of tremendous importance for modern astrophysics. Because of strong occultation, only the very top of the flaring loop was observed in the radio range, which implies that the observed source is reasonably uniform, so we can apply the uniform source model without explicitly considering the radiation transfer. We took the source parameters derived from HXR by Krucker et al. (2010) and selected a few underconstrained parameters to have some typical values and sent them to our GS code calculating the radio emission. As is apparent from Figure 9, the model radio emission is in excellent agreement with the observed one. This means that the same electron population needed to produce the HXR with the same spectral index extended to radio-producing

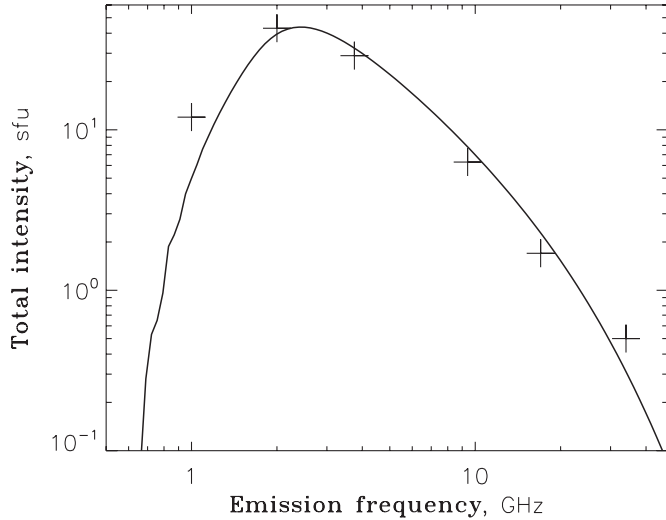


**Figure 9.** Model (solid) and observed (crosses) radio spectra for the solar flare of 2007 December 31. The spectra are plotted by IDL program Flare071231a.pro which is available in the online version of the journal; the list of simulation parameters is given in this program. The data point at 34 GHz is kindly provided by Dr. S. M. White.

energies (a few MeV) is fully consistent with the source radio properties.

However, the radio data analysis is not just a cross-check for the HXR diagnostics; in addition to it, the radio diagnostics put further constraints on such source parameters as the magnetic field, the viewing angle, the highest energy of accelerated electrons, and on the angular distribution of the fast electrons (e.g., Fleishman et al. 2009). Note that to obtain a reasonable “by eye” fit of the data by the model spectrum presented in this figure, we selected the mentioned parameters (see the full parameter list online in the IDL program Flare071231a.pro) from reasonable ranges and adopted a moderate loss-cone anisotropy similar to that observed for a number of radio loop-top sources (Melnikov et al. 2002) of extended flaring loops; an efficient account of the anisotropy, as has already been said, would not have been possible without the codes developed. A small excess of the observed flux compared with the model spectrum at 1 GHz (if not related to an observation error or a radio model uncertainty) could easily be provided by a minor source nonuniformity which is known to broaden the GS spectrum.

## 6. DISCUSSION AND CONCLUSIONS

In this paper, we present a set of GS codes, which allows a smooth transition from an exact (but often computationally demanding) GS code to approximate (but much faster and still highly precise) codes, where the computation time can be substantially reduced at the expense of very modest (if any) reduction of the computation accuracy applicable to both isotropic and anisotropic angular distributions of fast electrons. Specifically, the computation time is reduced by orders of magnitude, while the computation error remains within 1%–10% depending on the fast code option and parameter combination.

The importance of this development is difficult to overestimate: the reduction of computation time makes it widely applicable to create and analyze sophisticated models of GS radiation produced in realistic three-dimensional configurations. It was impossible until now because the long time required to compute a single GS spectrum from an anisotropic electron distribution made the solution of the whole problem prohibitively

slow. As a result, very few realistic three-dimensional GS models have yet been developed. Having the fast GS codes readily available enables analyzing many more interesting geometries and parameter combinations and thus a better understanding of how the GS spectra and images relate to the underlying source parameters and their evolution.

The software implementation developed for the fast GS codes is performed in a way complementary to the standard HXR tools. In particular, the same list of widely used model distribution functions is built into our codes, which allows a user to choose the same electron distribution function for both HXR and radio modeling from the set of predefined model functions and then vary the distribution parameters of interest. A combined analysis of the hard X-ray and radio observations (as has been shown in the example considered in the previous section) is a straightforward way of constraining the source parameters and testing the models of solar flares and other phenomena involving energetic particles.

Then, the fast codes are suitable for inclusion into the forward fitting inversion codes as the source functions (Fleishman et al. 2009). This may have a science-transforming effect because the possibility to use an arbitrary pitch-angle anisotropy in the trial fitting function paves the way for diagnosing both energy and angular distributions of the fast electrons accelerated in solar flares along with the magnetic fields (Fleishman et al. 2009) and so developing a remote sensing method for solar flares and other phenomena revealing themselves via GS emission.

This work was supported in part by NSF grants ATM-0707319, AST-0908344, and AGS-0961867 and NASA grant NNX10AF27G to the New Jersey Institute of Technology, and by the Russian Foundation for Basic Research grants 08-02-92204, 08-02-92228, 09-02-00226, and 09-02-00624. A.K. thanks the Leverhulme Trust for financial support. We thank Dr. Tim Bastian, NRAO, for stimulating discussions on the subject and also for valuable numeric input. We are highly grateful to the Nobeyama Observatory, Japan, for the invitation and support of our short-term visits to the Observatory where key steps of the reported work were performed. We thank Professor Kiyoto Shibasaki for his persistent encouragement of this work and Dr. Stephen White for helpful discussions of Nobeyama radio observations. We have made use of NASA’s Astrophysics Data System Abstract Service.

## APPENDIX A DISPERSION OF THE MAGNETOIONIC MODES

The refraction index of the electromagnetic waves in a plasma satisfies the dispersion equation

$$n_\sigma^2 = 1 - \frac{2v(1-v)}{2(1-v) - u \sin^2 \theta + \sigma \sqrt{\mathcal{D}}}, \quad (\text{A1})$$

where

$$\mathcal{D} = u^2 \sin^4 \theta + 4u(1-v)^2 \cos^2 \theta, \quad (\text{A2})$$

$$u = \left( \frac{f_{\text{Be}}}{f} \right)^2, \quad v = \left( \frac{f_{\text{pe}}}{f} \right)^2, \quad (\text{A3})$$

$f_{\text{pe}} = e\sqrt{N}/(\pi m_e)$  is the electron plasma frequency, and  $N$  is the total number density of the plasma electrons. For  $X$ -mode,  $\sigma = -1$ ; for  $O$ -mode,  $\sigma = +1$ .

The polarization vectors of the waves in the reference frame with  $z$ -axes along the magnetic field and the wave-vector  $\mathbf{k}$  in the  $(xz)$ -plane, has the form

$$\mathbf{e}_\sigma = \frac{(T_\sigma \cos \theta + L_\sigma \sin \theta, i, -T_\sigma \sin \theta + L_\sigma \cos \theta)}{\sqrt{1 + T_\sigma^2 + L_\sigma^2}} \quad (\text{A4})$$

with the parameters  $T_\sigma$  and  $L_\sigma$  defined as

$$T_\sigma = \frac{2\sqrt{u}(1-v)\cos\theta}{u\sin^2\theta - \sigma\sqrt{D}}, \quad (\text{A5})$$

and

$$L_\sigma = \frac{v\sqrt{u}\sin\theta + T_\sigma uv\sin\theta\cos\theta}{1-u-v+uv\cos^2\theta}. \quad (\text{A6})$$

Electromagnetic waves can propagate in plasma if their frequency exceeds the cutoff frequency,  $f > f_{c\sigma}$ , where

$$f_{c0} = f_{pe}, \quad f_{cx} = \frac{f_{Be}}{2} + \sqrt{f_{pe}^2 + \frac{f_{Be}^2}{4}}. \quad (\text{A7})$$

## APPENDIX B CODE IMPLEMENTATION

Fast GS codes were implemented as Windows DLLs and Linux SOs callable from IDL. Basically, we developed two variants of the libraries with the following file names:

1. libGS\_Std\_HomSrc\_C and
2. libGS\_Std\_HomSrc\_CEH.

The file extension depends on the target operation system. In the above names, Std refers to “standard” or pre-defined distribution functions (we are working on developing similar codes for arbitrary distributions given, e.g., by arrays of values), and HomSrc refers to “homogeneous source” (we are working on developing the codes with numerical integration of the radiation transfer equation for inhomogeneous sources). The last letters in the file names refer to the supported code modes: continuous (C), exact + approximate discrete (E), and hybrid (H).

Currently, the set of pre-defined distributions includes nine types of distributions over energy and five types of distributions over pitch angle; any combination of the energy and angular distribution is possible. The following energy distributions are implemented:

1. thermal (THM);
2. single power law over kinetic energy (PLW);
3. double power law over kinetic energy (DPL);
4. thermal/nonthermal over kinetic energy (TNT);
5. kappa (KAP);
6. power law over the absolute value of momentum (PLP);
7. power law over the Lorentz factor (PLG);

8. thermal/nonthermal over the absolute value of momentum (TNP); and
9. thermal/nonthermal over the Lorentz factor (TNG).

The following pitch-angle distributions are implemented:

1. isotropic (ISO);
2. exponential loss-cone (ELC);
3. Gaussian loss-cone (GLC);
4. Gaussian (GAU); and
5. super-Gaussian (SGA).

The detailed description of the pre-defined distributions is given in supplement I which is available in the online version of the journal. The calling sequence for our GS codes (for IDL users), input and output parameters, and keys to switch between the different code versions as well as minor differences between the above libraries are given in supplement II which is also available in the online version of the journal.

## REFERENCES

- Altyntsev, A. T., Fleishman, G. D., Huang, G.-L., & Melnikov, V. F. 2008, *ApJ*, **677**, 1367
- Bastian, T. S. 2006, in ASP Conf. Ser. 358, Solar Polarization 4, ed. R. Casini & B. W. Lites (San Francisco, CA: ASP), **173**
- Bastian, T. S., Benz, A. O., & Gary, D. E. 1998, *ARA&A*, **36**, 131
- Benka, S. G., & Holman, G. D. 1994, *ApJ*, **435**, 469
- Dulk, G. A. 1985, *ARA&A*, **23**, 169
- Dulk, G. A., & Marsh, K. A. 1982, *ApJ*, **259**, 350
- Eidman, V. Y. 1958, Sov. Phys.—JETP, **7**, 91
- Eidman, V. Y. 1959, Sov. Phys. JETP, **9**, 947
- Fleishman, G. D. 2006, in Proc. Nobeyama Symp. 2004, Solar Physics with the Nobeyama Radioheliograph, ed. K. Shibasaki et al. (NSRO Rep. 1; Nobeyama: Nobeyama Sol. Radio Obs.), **51**
- Fleishman, G. D., Gary, D. E., & Nita, G. M. 2003, *ApJ*, **593**, 571
- Fleishman, G. D., & Melnikov, V. F. 2003a, *ApJ*, **587**, 823
- Fleishman, G. D., & Melnikov, V. F. 2003b, *ApJ*, **584**, 1071
- Fleishman, G. D., Nita, G. M., & Gary, D. E. 2009, *ApJ*, **698**, L183
- Getmantsev, G. G. 1952, Dokl. Akad. Nauk SSSR, **83**, 557
- Ginzburg, V. L., & Syrovatskii, S. I. 1965, *ARA&A*, **3**, 297
- Ginzburg, V. L., & Syrovatskii, S. I. 1969, *ARA&A*, **7**, 375
- Holman, G. D., & Benka, S. G. 1992, *ApJ*, **400**, L79
- Klein, K.-L. 1987, *A&A*, **183**, 341
- Korchak, A. A. 1957, Sov. Astron., **1**, 360
- Korchak, A. A., & Terletsky, Y. P. 1952, Zh. Eksp. Teor. Fiz., **22**, 507
- Krucker, S., Hudson, H. S., Glesener, L., White, S. M., Masuda, S., Wuelser, J.-P., & Lin, R. P. 2010, *ApJ*, **714**, 1108
- Lee, J., & Gary, D. E. 2000, *ApJ*, **543**, 457
- Melnikov, V. F., Shibasaki, K., & Reznikova, V. E. 2002, *ApJ*, **580**, L185
- Melrose, D. B. 1968, *Ap&SS*, **2**, 171
- Petrosian, V. 1981, *ApJ*, **251**, 727
- Preka-Papadema, P., & Alissandrakis, C. E. 1992, *A&A*, **257**, 307
- Press, W. H., Teukolsky, S. A., Vetterling, W. T., & Flannery, B. P. 1997, Numerical Recipes in C: The Art of Scientific Computing (2nd ed.; Cambridge: Cambridge Univ. Press)
- Ramaty, R. 1969, *ApJ*, **158**, 753
- Razin, V. A. 1960, Izv. VUZov. Radiofiz., **3**, 584
- Reznikova, V. E., Melnikov, V. F., Shibasaki, K., Gorbikov, S. P., Pyatakov, N. P., Myagkova, I. N., & Ji, H. 2009, *ApJ*, **697**, 735
- Syrovatskii, S. I. 1959, AZh, **36**, 17
- Tzatzakis, V., Nindos, A., & Alissandrakis, C. E. 2008, *Sol. Phys.*, **253**, 79
- Wild, J. P., & Hill, E. R. 1971, Aust. J. Phys., **24**, 43